Journal of Solid State Chemistry 187 (2012) 20–26

Contents lists available at SciVerse ScienceDirect

Journal of Solid State Chemistry

journal homepage: www.elsevier.com/locate/jssc

Synthesis of high intrinsic loss power aqueous ferrofluids of iron oxide nanoparticles by citric acid-assisted hydrothermal-reduction route

Behshid Behdadfar [a,*], Ahmad Kermanpur [a], Hojjat Sadeghi-Aliabadi [b], Maria del Puerto Morales [c], Morteza Mozaffari [d]

[a] Department of Materials Engineering, Isfahan University of Technology, Isfahan 84156-83111, Iran
[b] School of Pharmacy, Isfahan Pharmaceutical Research Center, Isfahan University of Medical Sciences, Isfahan, Iran
[c] Instituto de Ciencia de Materiales de Madrid, CSIC, Cantoblanco 28049, Madrid, Spain
[d] Department of Physics, Razi University, Kermanshah, Iran

ARTICLE INFO

Article history:
Received 7 August 2011
Received in revised form
8 December 2011
Accepted 9 December 2011
Available online 19 December 2011

Keywords:
Hydrothermal-reduction route
Iron oxide nanoparticles
Aqueous ferrofluids
Intrinsic loss power
Magnetic hyperthermia
Environmental friendly method

ABSTRACT

Monodispersed aqueous ferrofluids of iron oxide nanoparticle were synthesized by hydrothermal-reduction route. They were characterized by X-ray diffraction analysis, Fourier transform infrared spectroscopy, scanning and transmission electron microscopy and dynamic light scattering. The results showed that certain concentrations of citric acid (CA) are required to obtain only magnetic iron oxides with mean particle sizes around 8 nm. CA acts as a modulator and reducing agent in iron oxide formation which controls nanoparticle size. The XRD, magnetic and heating measurements showed that the temperature and time of hydrothermal reaction can affect the magnetic properties of obtained ferrofluids. The synthesized ferrofluids were stable at pH 7. Their mean hydrodynamic size was around 80 nm with polydispersity index (PDI) of 0.158. The calculated intrinsic loss power (ILP) was 9.4 nHm^2/kg. So this clean and cheap route is an efficient way to synthesize high ILP aqueous ferrofluids applicable in magnetic hyperthermia.

1. Introduction

Magnetic nanoparticles have many applications in biomedical sciences and industries due to their convenient physical characteristics[1,2]. Among different kinds of magnetic nanoparticles, investigations have been focused on iron oxide nanoparticles due to their better chemical stability and biocompatibility compared to other metallic magnetic nanoparticles [3,4].

Development of large scale production methods of uniform iron oxide nanoparticles, compatible with health and environment, is still a challenge. Many methods have been developed to synthesize iron oxide nanoparticles [5]. Wet coprecipitation method is widely used to prepare the iron oxide nanoparticles, but the main disadvantage of this method is the wide size distribution of the resulting nanoparticles [6]. Thermal decomposition of organometallic precursors in organic solvents at high temperatures in the presence of surfactants is widely used for the synthesis of monodispersed iron oxide nanoparticles [7]. But the nanoparticles prepared by this method are not hydrophilic in nature and they cannot be dispersed in water which limits their biomedical applications [8]. Therefore many investigations have focused on the preparation of biocompatible aqueous ferrofluids containing controllable sizes having good magnetic properties by soft-chemical routes [8,9].

Many methods have been developed to coat iron oxide nanoparticles by organic or inorganic and biocompatible layers to stabilize them in aqueous medium and also to install accessible surface sites for conjugation of biomolecules [4]. Small molecules are very attractive due to their ease of preparation and simple chemical conjugation [10,11]. Among different small molecules, citrate ions have been extensively used to coat iron oxide nanoparticles which lead to a stable aqueous ferrofluids. Recently, Liu et al. [12] fabricated highly water-dispersible magnetite nanoparticles with a uniform size by solvothermal reaction at 200 °C by reduction of $FeCl_3$ with ethylene glycol in presence of trisodium citrate as a stabilizer. Munnier et al. [13] prepared citrate-stabilized iron oxide nanoparticle by agitating bare nanoparticles in CA solution. Khosroshahi and Ghazanfari [14] fabricated citrate modified Fe_3O_4 nanoparticles by stirring bare Fe_3O_4 nanoparticles in trisodium citrate solution as inter mediate to obtain silica-coated magnetite core-shell nanoparticles. However, most of these works on fabrication of aqueous stabilized iron oxide nanoparticle involved multiple synthesis steps [13,15,16].

Hydrothermal-reduction method is an easy and one step route to prepare hydrophilic magnetite nanoparticles with different precursors. Zheng et al. [17] fabricated magnetite nanoparticles by

* Corresponding author. Fax: +98 311 3912752.
E-mail address: bbehdadfar@ma.iut.ac.ir (B. Behdadfar).

0022-4596/$ - see front matter © 2011 Elsevier Inc. All rights reserved.
doi:10.1016/j.jssc.2011.12.011

reduction of $Fe(NO_3)_3 \cdot 9H_2O$, using hydrazine as reducing agent in the presence of a surfactant as stabilizer. Furthermore, a $(NH_4)_2SO_4$–$FeSO_4 \cdot 6H_2O$ precursor in the presence of hydrazine was also exploited for the formation of iron oxides [18]. Park [19] used ammonium iron citrate ($C_6H_8O_7$–nFe–nH_3N) as a precursor for preparing iron oxide nanoparticles. Other reductants, reported in the literature, are sodium borohydride ($NaBH_4$) [20], carbon monoxide (CO) [21] and dimethyl formamide (DMF) [22]. All of these reductants are highly reactive chemicals and pose potential environmental and biological risks. Then recently mild and nontoxic reducing agents such as ascorbic acid [23], tartaric acid [24], aspartic acid [25] and α-D glucose [26] have been used in synthesizing iron oxide nanoparticles by hydrothermal-reduction method.

In this work, isolated iron oxide nanoparticles with sizes around 9 nm have been synthesized in water using the hydrothermal-reduction method in the presence of citric acid (CA) as a non-expensive and non-toxic reducing agent and stabilizer. CA and an iron (III) salt were the only precursors to produce uniform iron oxide nanoparticles. The synthesized nanoparticles were stable in water at pH 7 and their intrinsic loss power (ILP) was higher than that of commercial ones assuring their application in magnetic hyperthermia.

2. Materials and methods

2.1. Materials

All raw materials, including $Fe(NO_3)_3.9H_2O$, NH_4OH 25% and $C_6H_8O_7.H_2O$, were purchased from Merck Co. with minimum purities of 99%.

2.2. Synthesis

In a typical experiment, 12 mmols of $Fe(NO_3)_3 \cdot 9H_2O$ were dissolved in 25 ml of deionized distilled water under continuous stirring. After 10 min stirring, a solution of NH_4OH 25% was added slowly to reach a medium pH of 9. Vigorous stirring continued for another 10 min and a reddish brown slurry was obtained. The slurry was then centrifuged and washed three times with deionized distilled water to remove excess ions and reach a pH medium of 7. To optimize concentration of CA, different concentrations of CA (4, 8, 16 and 22 mM) were added to the iron oxide precursors. The mixtures were stirred vigorously for 10 min and then transferred into a 500 ml volume teflon-lined autoclave. The autoclave was kept at 180 °C for 20 h and then free-cooled to room temperature. The products were named A, B, C and D for different CA concentrations 4, 8, 16 and 22 mM, respectively.

Ferrofluids from samples C and E were prepared by washing the precipitate with acetone, mixing with 10 ml of deionized distilled water and sonicated for 10 min. The black suspensions were centrifuged for 10 min with a speed of 6000 rpm and acceleration of 1500*g*. The supernatants were the desired ferrofluids and the remaining nanoparticles aggregated at the bottom of the tubes were discarded. For powder characterization, the precipitate was washed with acetone via magnetic decantation several times and then freeze dried at −70 °C and 0.2 mbar pressure.

To investigate the effects of reaction time and temperature on structure and phase formation of iron oxide nanoparticles, some samples with the optimum concentration of CA were synthesized at 200 °C and soaking times from 10 to 20 h.

2.3. Characterization

The morphology, particle size and distribution were investigated using a transmission electron microscope (JEOL-2000 FXII) operating at 200 keV. A drop of the suspensions was deposited on a carbon coated copper grid and left to dry at room temperature. Mean particle size was calculated from TEM data by measuring the size of at least 300 particles. The data were fitted to a log-normal distribution and then the mean size and the polydispersity degree were obtained from it.

Morphology of the nanoparticles was investigated by a Philips, XL30 SEM.

Phase identification was carried out using a Bruker, D8 ADVANCED model, using Cu$K\alpha$ radiation ($\lambda = 1.5406$ Å). Scherrer's formula ($d = 0.9\lambda/\beta \cos\theta$) was used to estimate the crystallite size (d) of the samples with full-width at half-maximum value (β) obtained from the (311) peak [27].

Fourier transform infrared spectra were recorded between 3600 and 400 cm^{-1} using a Jasco FTIR-680 plus spectrophotometer. Samples were prepared by diluting the iron oxide nanoparticles in KBr at 2% by weight and pressing it into a pellet.

The thermogravimetric analysis of the samples was carried out using a SEIKO TG/ATD 320 U, SSC 5200. The analysis was performed from room temperature to 900 °C at 10 °C/min in air flow. The analysis of the weight loss percentage allows the quantification of the coating.

Colloidal properties of the aqueous suspensions (mean hydrodynamic size, polydispersity index and zeta potential) were obtained by dynamic light scattering (DLS) using a Malvern instrument Zetasizer (DTS Ver. 5.02). The diluted samples dispersed in deionized distilled water at 1 mg Fe/ml, were used in this study. The hydrodynamic size was measured at pH 7 and the intensity data were analyzed to obtain the Z-average size (Cumulants mean) and the intensity, volume and number distributions. Z-potential was measured with 0.01 M concentration of KNO_3 at different pH values between 2 and 12.

Magnetic measurements were carried out by a vibrating sample magnetometer (MLVSM9 MagLab 9 T, Oxford Instrument). Samples were prepared by packing the powders into pellets. Magnetization curves were recorded at room temperature by first saturating the sample in a field of 5 T. The magnetization values were normalized to the amount of iron to yield the specific magnetization (emu/g Fe_3O_4). M_s values were extrapolated from the high field part of the measured magnetization curve, where the magnetization increases with 1/H linearly, when it tends to zero.

To measure the initial linear rise in temperature as a function of time (dT/dt), a homemade radio-frequency (RF) power supply was connected to an induction coil (Fig. 1). The coil was made of copper tube with 6 mm in diameter and had 8 turns and a diameter of 5 cm. The temperature was probed with an alcoholic thermometer to prevent the thermal effects related to the alternative magnetic field. Frequency of the alternative magnetic field was 330 kHz and the input power to the coil was 6.4 kW. The intensity of magnetic field in the center of the coil was estimated to be 6 kA/m. The prepared ferrofluid consisting of 5 mg iron

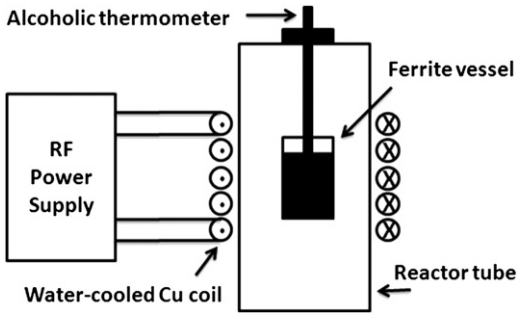

Fig. 1. Schematic diagram of set-up used for measurement of specific loss power.

oxide dispersed in 1 ml of deionized distilled water was put in a glass vessel which was isolated, using a teflon shell. The specific loss power (SLP) is defined as the thermal power dissipation divided by the mass of magnetic component and can be expressed as [6]:

$$SLP = \sum[(C_i m_i + A)/m]\ dT/dt \quad (1)$$

where C_i is the specific heat capacity of the ith component of ferrofluid, m_i is the mass of the component, A is water equivalent of the tube and alcoholic thermometer ($A = 11.28$ J/K) and m is the mass of iron oxide in the ferrofluid. Specific heat capacities of distilled water and magnetite are 4180 and 650 J/kg K, respectively [8]. In all experiments, only deionized distilled water was kept in the glass vessel for 30 min at the same field intensity and the temperature was measured by the same alcoholic thermometer. The temperature did not rise when only water was kept inside the coil.

To allow more direct comparisons to be made between SLP measurements performed in different laboratories and under different AC field strength and frequency conditions, intrinsic loss power (ILP) has been defined as [28]

$$ILP = SLP/H^2 f \quad (2)$$

This equation is valid under frequencies of up to several MHz; samples with a PDI of more than 0.1 and also provided the applied field strength H is well below the saturation field of the magnetic nanoparticles.

3. Results and discussion

3.1. Structural and colloidal properties of nanoparticles

Fig. 2 shows XRD patterns of the synthesized samples at 180 °C and soaking time of 20 h with different concentrations of CA and 24 mM Fe^{3+} ions (Table 1). As it can be seen, all main peaks on the XRD pattern of the sample with the lowest CA concentration (4 mM) are related to hematite, except for some low intensity peaks assigned to the spinel structure (Fig. 2A). This result is consistent with the result of investigation done by Schwertmann and Murad [29] showing the high probability of transformation of ferrihydrite to hematite in a medium pH between 6 and 9. With increasing CA concentration, the products change from hematite to magnetite gradually. For a CA concentration equal to or higher than 16 mM, the products are single phase magnetite (Fig. 2C and D). The mechanism of the formation of magnetite in this process can be explained by the results of former works: Sulzberger et al. [30], showed that at the surface of ferrihydrite in water medium, functional OH groups are able to interact with reductant ligands such as oxalate or CA. These ligands become bound to the Fe^{3+} centers at the surface of the oxide, which act as Lewis acids. In relatively fast ligand exchange reaction surface OH^- ions are replaced, e.g. by the anion of the reductant. In this case the reductant can readily exchange electrons with a Fe^{3+} surface center. The electron transfer leads to an oxidized reactant (often radical) and a surface Fe^{2+} ion. Tronc et al. [31] showed that in normal condition (not hydrothermal) after formation of Fe^{2+} ions on the surface of ferrihydrite, electron transfer takes place between Fe^{2+} and Fe^{3+} ions which plays a fundamental role in the formation of spinel iron oxide even at low Fe^{2+} levels. From the XRD patterns it can be deduced that in the presence of CA, Fe^{3+} ions on the precursor surface can be reduced to Fe^{2+} ions leading to the formation of magnetite. The extent of reduction depends on the CA concentration. When concentration of CA is low, only few Fe^{3+} ions are reduced to Fe^{2+} ions, so the amount of produced magnetite is low and the Fe^{3+} precursors evolute to hematite due to the pH of the reaction medium which is near 6 for samples with lower concentrations of CA [29]. But as the concentration of CA is increased, the amount of Fe^{2+} ions increases. These ions act as catalyst in the production of magnetite via electron transfer from surface Fe^{2+} ions to neighboring inner Fe^{3+} ions in the precursors structure through metal–metal bonding which is likely to be thermally assisted. Hence the structure of precursors is transformed to the spinel structure [31]. Further addition of CA resulted in a smaller height of the spinel peaks and larger widths (Fig. 2D). This indicated that excess amounts of CA in the reaction medium inhibited the magnetite crystal growing via chelating the iron ions. Scherrer's formula was used to estimate the crystallite size of the samples C and D, which were 8.3 and 6.5 nm, respectively. Then sample C was chosen as better one among these two samples because of its higher specific loss power, which will be discussed in Section 3.2 briefly.

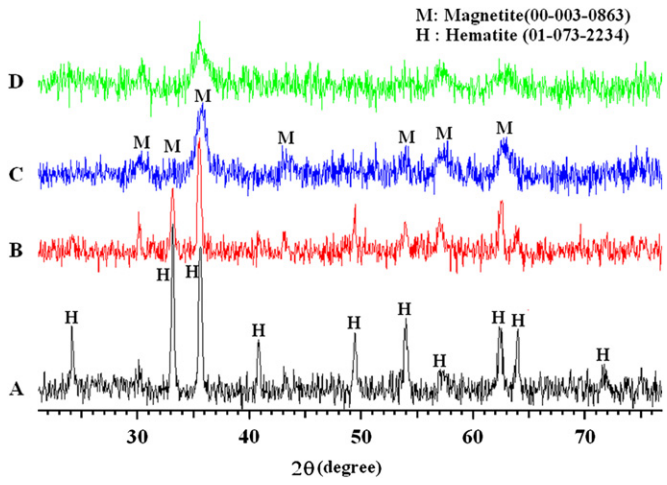

Fig. 2. XRD patterns of the synthesized samples with different CA concentrations: (a) 4, (b) 8, (c) 16 and (d) 22 mM.

Table 1
Synthesis parameters for different samples.

Sample	CA/Fe^{3+}	Hydrothermal temperature (°C)	Soaking time (h)
A	0.16	180	20
B	0.33	180	20
C	0.67	180	20
D	0.92	180	20
E	0.67	200	10

To investigate the effects of reaction time and temperature on structure and phase formation of iron oxide nanoparticles, some samples with the same concentration of CA as sample C were synthesized at 200 °C and soaking times from 10 to 20 h. For the reaction time of 20 h the resulting iron oxide nanoparticle sizes were too large to form stable ferrofluids. So the reaction time was decreased to synthesize nanoparticles with smaller sizes. The optimum reaction time for 200 °C was 10 h. The sample prepared in this condition was named E (Table 1). Table 2 shows the measured and calculated characteristics of both samples C and E.

XRD pattern of sample E is shown in Fig. 3b. In X-ray diffraction pattern seven intense peaks are indexed by (200), (220), (311), (400), (422), (511) and (440), which are matched with Fe_3O_4 (00-003-0863) and γ-Fe_2O_3 (00-004-0755) phases. It is not easy to tell whether the product is either Fe_3O_4 or γ-Fe_2O_3, but because of black color of the sample it can be concluded that most part of the sample is compose of magnetite [32]. Calculated crystallite size of sample E was 8.2 nm.

Table 2
Measured and calculated characteristics of samples C and E iron oxide nanoparticles.

Sample	M_s, *RT* (emu/g)	Coercivity at RT (Oe)	M_s 5 K (emu/g)	Coercivity at 5 K (Oe)	XRD crystallite size (nm)	TEM mean particle size (nm)	DLS hydrodynamic size (nm) (PDI)	Particle concentration (mg/ml)	SLP (W/g)	ILP (nHm^2/kg)
C	65.77	0	81.9	210	8.3	8.4 ± 2.5	167(0.2)	5	10.86	0.9
E	66.3	30	74	275	8.2	9.5 ± 2.8	77(0.158)	2.5	111.76	9.4

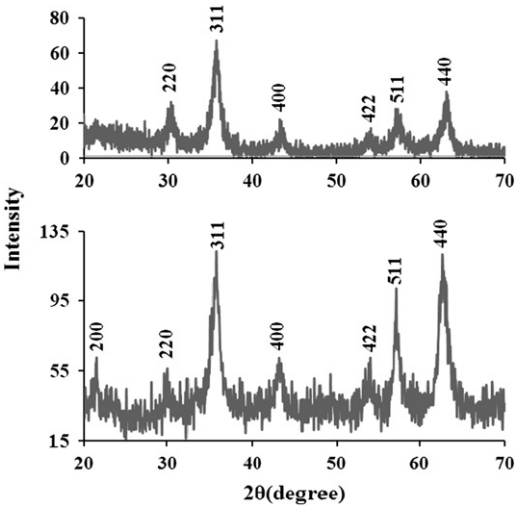

Fig. 3. XRD patterns of iron oxide nanoparticles (a) sample C and (b) sample E.

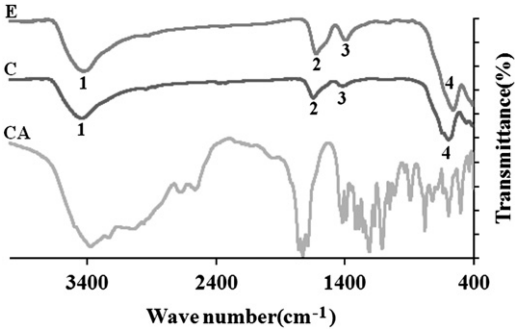

Fig. 4. FTIR spectra of CA and citrate coated iron oxide nanoparticles of samples C and E.

Presence of citrate ions on the surface of iron oxide nanoparticles was revealed by FTIR spectroscopy. Fig. 4 shows FTIR spectra of CA, samples C and E. Peak 1 of samples C and E can be assigned to the structural OH. In the CA spectrum the 1690–1760 cm^{-1} strong peak shows the C=O vibration (symmetric stretching) from the COOH group of CA. For the iron oxide nanoparticles coated with CA this peak has shifted to 1627 cm^{-1}, so peak 2 of samples C and E can be assigned to binding of a CA radical to the iron oxide nanoparticle surface. Peak 3 of two samples indicates the asymmetric stretching of CO from the COOH group. Peak 4 is the characteristic peak of magnetic iron oxide [33].

Quantification of the coating was carried out by TG analysis. The results for samples C and E showed weight losses in three steps (Fig.5). A weight loss of about 5.5% for sample C and 3.2% for sample E below 100 °C can be ascribed to the removal of physically adsorbed water molecules from the surface of magnetic nanoparticles. This shows that the total water loss of these samples depends on the temperature of the hydrothermal synthesis. In other words at higher synthesis temperatures, the number

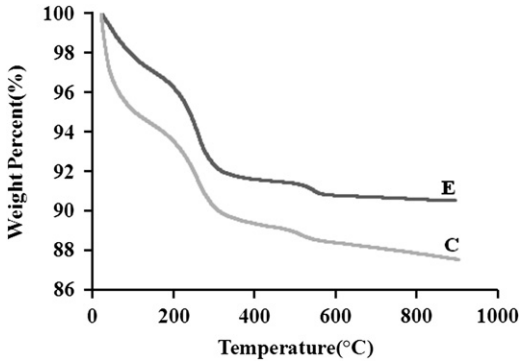

Fig. 5. TGA curves of the samples C and E.

of remaining hydroxyl groups on the particle surface strongly decreases, so sample C which is synthesized at 180 °C contains more hydroxyl groups on its particles surfaces than the sample E which is synthesized at 200 °C, leading to form greater aggregates in sample C [34]. Due to the presence of one step weight loss in neat CA at about 200 °C [35], the weight loss of about 5% for sample C and 5.8% for sample E about 255 °C can be associated with the removal of chemically attached CA molecules from the surface of iron oxide nanoparticles leading to form smaller aggregates and hydrodynamic size in sample E. The small weight loss beyond 500 °C is associated with the phase transformation of iron oxide to hematite for both samples.

Uniformity in size and shape of the iron oxide nanoparticles obtained by this method can be observed in the SEM and TEM images of the sample C (Fig. 6a–d) and the TEM images of sample E (Fig.7a and b). Mean particle sizes which were calculated from TEM data were 8.4 nm with a standard deviation of 2.5 nm for sample C (Fig.6e) and 9.5 nm with a standard deviation of 2.8 nm for sample E (Fig.7c). The larger average size of sample E can be attributed to the higher temperature of synthesis procedure and affects the magnetic properties and hence loss power of the ferrofluids which will be discussed in Section 3.2.

Colloidal properties of the ferrofluids prepared from samples C and E are shown in Figs. 8 and 9. The hydrodynamic size distribution in intensity data at pH 7 was obtained using the DLS. The Z-average sizes were 167.3 and 77 nm with polydispersity indices of 0.23 and 0.158 for samples C and E, respectively (Fig.8), confirming the formation of smaller aggregates in sample E which is in agreement with TGA experiments. As the polydispersity index can vary from 0.01 up to 0.5 [36], it can be concluded that the resulting ferrofluids prepared from these iron oxide nanoparticles are rather monodispersed. Zeta potential measurements at different pH values between 2 and 12 (Fig.9) showed that the ferrofluids of samples C and E at pH 7 had negative surface potentials of around −20 and −30 mV, respectively, which confirms the presence of citrate ions on the surface of iron oxide nanoparticles assuring a longer term stability of the ferrofluids of sample E at pH 7. It may be because of more citric acid and less hydroxyl groups concentration on the surface of nanoparticles according to TGA experiments. The isoelectric

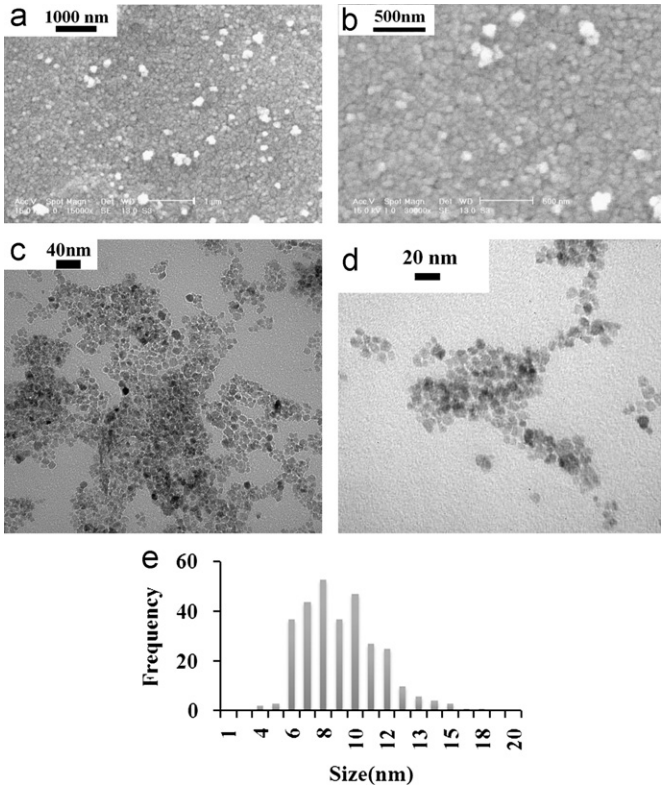

Fig. 6. (a,b) SEM, (c,d) TEM images of the synthesized nanoparticles of sample C with different magnifications and (e) nanoparticle size histogram for sample C.

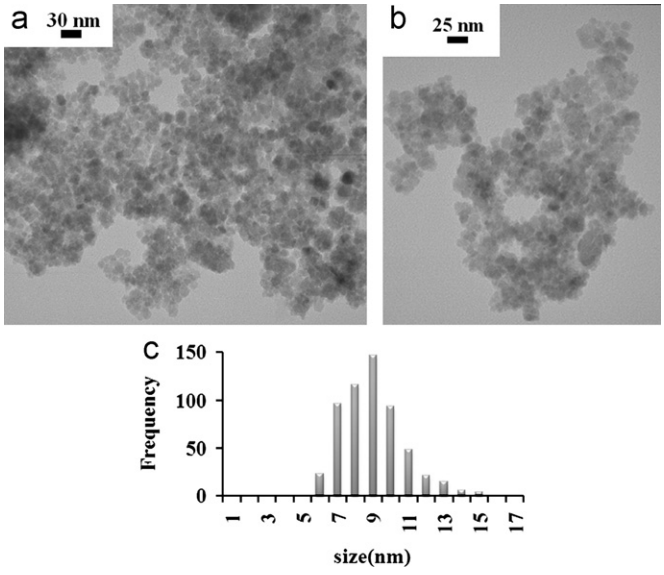

Fig. 7. (a,b) TEM images of the synthesized nanoparticles of sample E with different magnifications and (c) nanoparticle size histogram for sample E.

points of the nanoparticles of the samples C and E were around pH 4.5 and 2.5, respectively (Fig. 9).

3.2. Magnetic and heating properties of nanoparticles

Magnetic properties of the nanoparticles were analyzed at two different temperatures. Figs. 10 and 11 show *M–H* curves of the iron oxide nanoparticles, samples C and E, respectively, at 290 and 5 K. As it can be seen the nanoparticles of sample C are superparamagnetic at room temperature (zero remanence and

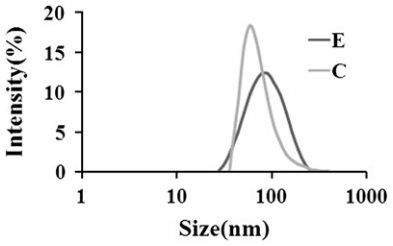

Fig. 8. Hydrodynamic size distributions of dispersed nanoparticles of samples C and E in aqueous media.

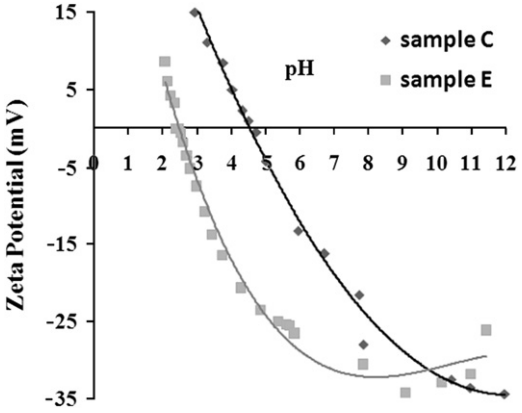

Fig. 9. Variation of surface potentials for iron oxide nanoparticles of samples C and E versus pH.

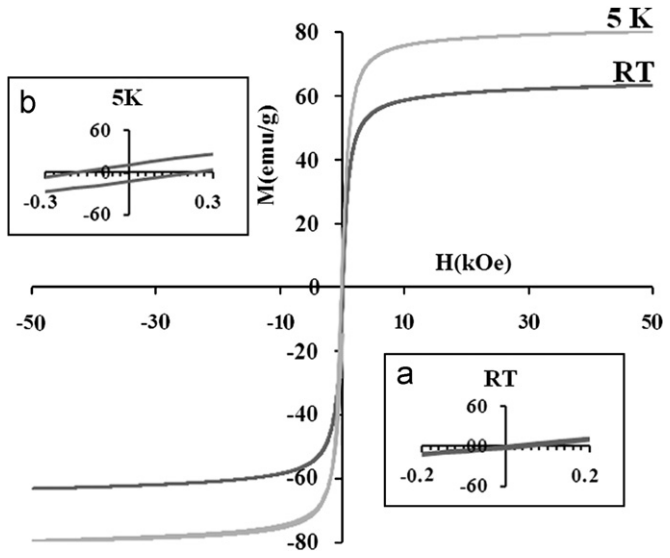

Fig. 10. *M–H* curves of iron oxide nanoparticles (sample C) at room temperature, and at 5 K, the insets of a and b show the low field parts.

coercivity) with a saturation magnetization of 65.77 emu/g. However, at 5 K there is a hysteresis loop with a coercivity of 210 Oe and a saturation magnetization of 81.9 emu/g. The reported value for the saturation magnetization of bulk magnetite at room temperature and at 0 K are 92 and 98 emu/g, respectively and for bulk maghemite are 76 and 83.5 at room temperature and at 0 K, respectively [37]. Fig.11 shows that the nanoparticles of sample E are not superparamagnetic at both room temperature and 5 K, where the coercivities are 30 and 275 Oe, respectively. This can be attributed to the larger average size of sample E nanoparticles which was calculated using TEM images (Figs. 6 and 7). The calculated saturation magnetizations of sample E are

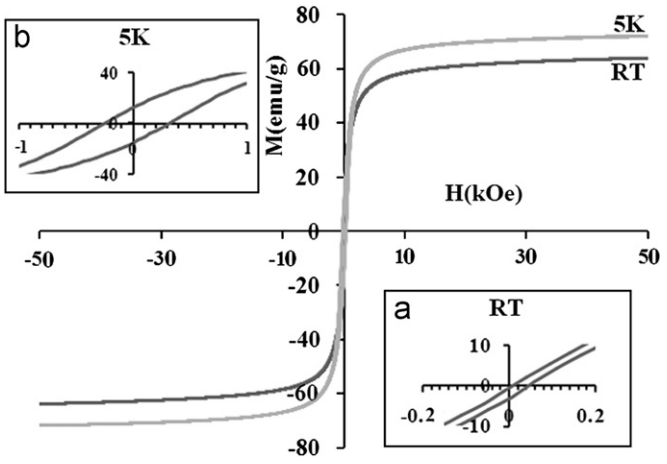

Fig. 11. *M–H* curves of iron oxide nanoparticles (sample E) at room temperature, and at 5 K, the insets of a and b show the low field parts.

66.3 and 74 emu/g at room temperature and 5 K, respectively. The results show that increasing temperature in hydrothermal–reduction reaction increases the magnetic anisotropy of the iron oxide nanoparticles. Saturation magnetization values obtained for both samples are within the reported values for magnetite particles of similar size prepared by thermal decomposition of organic precursors at 300 °C [38], but these are higher than those reported for magnetite nanoparticles prepared by coprecipitation method [6]. This can be due to their higher crystallinity which results from the hydrothermal synthesis method.

Magnetic nanoparticles can serve as colloidal mediators for heat generation by transforming the energy supplied by an external AC magnetic field into thermal energy. Heating properties of the particles prepared in this work have been evaluated by measuring the initial linear rise in temperature as a function of time (dT/dt) in an alternating magnetic field with an intensity of 6 kA/m and a frequency of 330 kHz. Calculated SLPs from eq.1 were 10.86 W/g for 5 mg iron oxide/ml ferrofluids of sample C and 111.76 W/g for 2.5 mg iron oxide/ml ferrofluids of sample E.

The SLP of single domain iron oxide nanoparticles in an external AC magnetic field can be attributed to two kinds of power loss mechanisms: hysteresis and relaxation losses [39]. These two power losses are functions of the particle size. For single domain nanoparticles without superparamagnetic characteristic, depending on their size, loss power can be caused by both mechanisms whereas for superparamagnetic nanoparticles only relaxation mechanisms are the main sources of loss power [39]. Relaxation losses are caused by the relaxation processes of single domain magnetic nanoparticles in an AC magnetic field, which are the gradual alignment of the magnetic moments during the magnetization process. The relaxation processes of a ferrofluid may take place through two distinct mechanisms. The first one consists of the rotation of the single domain nanoparticle, which is related to the Brownian motion of the magnetic nanoparticles. The second one corresponds to magnetization vector rotation if we abstract the Brownian motion and consider the particle immobile. The second one is the so-called Neel relaxation [40] of magnetic nanoparticles. Ferrofluids can exhibit both of these mechanisms, each having the proper weight. The power loss corresponding to Neel or Brown relaxation is approximately given by [40]:

$$P = (mH\omega\tau)^2/[2\tau kT\rho V(1+\omega^2\tau^2)] \quad (3)$$

where m is the particle magnetic moment, τ is the magnetic relaxation time (discussed below), ω the measurement angular frequency, ρ the density of magnetic nanoparticles and H the field intensity amplitude. The relaxation time of the Brownian motion is

$$\tau_B = 4\pi\eta r^3/kT \quad (4)$$

and the Neel relaxation time is

$$\tau_N = \tau_0 \ \exp(KV/kT) \quad (5)$$

where η is the basic liquid viscosity, r is the hydrodynamic radius of the particle, k is Boltzmann's constant, τ_0 is the time constant (10^{-9} s), K is the magnetocrystalline anisotropy energy density (1.35×10^4 J/m^3) and V is the particle volume. The measurement frequency defines the so called critical particle volume V_c for which $\omega\tau=1$. Near this critical size, relaxation effects cause a rapid decrease of the remanent magnetization. Consequently, hysteresis losses vanish abruptly near the critical particle size [40]. For our measuring frequency of 330 kHz critical particle size is about 15 nm which makes $\omega\tau_N=1$ and P_{Neel} reaches its maximum. For samples C and D grain sizes are 8.4 and 6.5 nm, respectively so the Neel loss is small for both samples C and D in the applied frequency; however, the Neel loss of sample C is comparatively higher than that of sample D. The narrow size distribution of sample C has not effective contribution to loss power because the average nanoparticle size of this sample does not lead to high loss power in the applied frequency and many particles cannot produce enough heat in this range of sizes, so sample E was synthesized in 200 °C and soaking time of 10 h to produce nanoparticles with larger average size. The higher value of SLP of sample E is due to the existence of coercivity and hence larger magnetic anisotropy in sample E which leads to an additional hysteresis loss in heat generation process if the applied magnetic field amplitude is large enough to exceed the coercivity of the majority of particles [41]. The applied magnetic field amplitude was 6 kA/m or equivalently 75 Oe which is higher than the coercivity of sample E (30 Oe). In this case the narrow size distribution of sample E causes a high SLP because many particles can reach their maximum SLP in the applied magnetic field amplitude.

With consideration $\omega\tau_B=1$ the optimum hydrodynamic size for our measuring frequency is 11 nm. The hydrodynamic sizes of samples C and E are 77 and 167 nm, respectively which are very different from the optimum hydrodynamic size. Brownian losses are both very small for samples C and E in the applied frequency.

The direct comparison of these data with other ferrofluids reported in literature is difficult due to different AC field strengths and frequencies used in the measurements. A new parameter has been recently introduced, the 'intrinsic loss power' (ILP), which allows more direct comparisons to be made between experiments performed in different laboratories and under different AC field strength and frequency conditions [28]. The heating efficiencies of our ferrofluids, evaluated from the ILP, were 0.9 and 9.4 nHm^2/kg for samples C and E, respectively. The best synthetic iron oxide particles in the literature to date were those reported by Fortin et al. [42] and Hergt et al.[43]. The former had a reported SLP parameter of 1650 W/g at $H=24.8$ kA/m and $f=700$ kHz, while the latter had an SLP of 600 W/g at 11.2 kA/m and 410 kHz. The system normalized ILP parameters for these samples are 3.8 and 11.7 nHm^2/kg, respectively. Kallumadil et al. [28] compared the ILP of some commercial ferrofluids with different hydrodynamic sizes. The ILP of micromode ferrofluids with the hydrodynamic sizes between 100 and 170 nm and particle sizes of about 7 nm vary from 0.15 to 0.35 nHm^2/kg. The ILP of Chemicell ferrofluids with hydrodynamic sizes 160 and 177 nm and particle sizes of about 9.5 nm are 1.41 and 1.31 nHm^2/kg, respectively. The highest ILPs between commercial ferrofluids belong to Micromode and Bayer-Schering ferrofluids which are 3.12 and 3.1 nHm^2/kg with hydrodynamic sizes of 91 and 61 nm and particle sizes of

Table 3
Comparison between ILP of samples C and E with ILP of some commercial ferrofluids reported in literature.

Manufacturer	Name	Coating	DLS hydrodynamic size (nm) (PDI)	Crystallite size (nm)	Intrinsic loss power ILP (nHm^2/kg)
Chemicell	Fluidmag-D	Starch	42 (0.13)	9.8	1.31 [28]
Micromod	Nanomag-D-Spio	Carboxyl	91 (0.13)	11.8	3.12 [28]
Micromod	BNF-01908	Starch	108 (0.08)	7.7	0.35 [28]
Chemicell	Fluidmag-D	Starch	109 (0.1)	10	2.01 [28]
Chemicell	Fluidmag-D	Starch	160 (0.18)	9.6	1.41 [28]
Chemicell	Fluidmag-NC-D	Starch	177 (0.18)	9.5	1.31 [28]
Chemicell	Fluidmag-NY-D	Starch	212 (0.17)	9.6	1.53 [28]
Chemicell	Fluidmag-CMX	Carboxy methyl dextran	220 (0.21)	9.9	1.71 [28]
Micromod	Nanomag-D-Spio	Carboxyl	346 (0.21)	8.9	0.37 [28]
Micromod	BNF-02008	Carboxyl	512 (0.14)	7.6	0.16 [28]
Bayer-Schering	Resovist	Carboxy dextran	61 (0.19)	10.5	3.1 [28]
Micromod	BNF-01708	Carboxyl	130 (0.08)	7.1	0.15 [28]
Micromod	Nanomag-D-Spio	Carboxyl	84 (0.15)	11.2	2.31 [28]
Micromod	Nanomag-D-Spio	Carboxyl	165 (0.05)	8.3	0.23 [28]
Chemicell	Fluidmag-D	Starch	39 (0.08)	12.6	2.67 [28]
Micromod	BNF-01808	Carboxyl	129 (0.12)	8.2	0.17 [28]
This work	C	Citric acid	167.3 (0.2)	8.4	0.9
This work	E	Citric acid	77 (0.158)	9.5	9.4

11.8 and 10.5 nm, respectively. Comparing our results with the results in that report shows that the ILP of sample E is higher than all the commercial ferrofluids and also from the most of ILPs reported in literature. Also the ILP of sample C is comparable and higher than ILPs of commercial ones with similar hydrodynamic sizes (Table 3).

4. Conclusion

Monodispersed aqueous ferrofluids of iron oxide nanoparticles with the mean hydrodynamic size of 77 nm and polydispersity index of 0.158 were successfully synthesized via single step hydrothermal-reduction route in the presence of CA as a reducing agent and stabilizer. This is a cheap, facile and environmental friendly method which leads to the formation of iron oxide ferrofluids with high intrinsic loss power, hence the iron oxide nanoparticles prepared by this route can be applicable in magnetic hyperthermia. It was concluded that CA had a reducing agent role in magnetic iron oxide formation via a hydrothermal-reduction process, moreover reaction temperature and time affect critically the average size and magnetic properties of synthesized nanoparticles and hence their heating efficiency.

References

[1] Z.L. Liu, et al., J. Magn. Magn. Mater. 283 (2–3) (2004) 258–262.
[2] M. Zahn, J. Nanopart. Res. 3 (1) (2001) 73–78.
[3] Z. Liu, J. Ding, J. Xue, New J. Chem. 33 (1) (2009) 88–92.
[4] J.R. McCarthy, R. Weissleder, Adv. Drug Deliv. Rev. 60 (11) (2008) 1241–1251.
[5] P. Tartaj, et al., J. Phys. D-Appl. Phys. 36 (13) (2003) R182–R197.
[6] R.A. Frimpong, et al., J. Magn. Magn. Mater 322 (3) (2010) 326–331.
[7] A.G. Roca, et al., Nanotechnology 17 (11) (2006) 2783–2788.
[8] S. Nigam, K.C. Barick, D. Bahadur, J. Magn. Magn. Mater. 323 (2) (2011) 237–243.
[9] K.C. Barick, et al., J. Magn. Magn. Mater. 321 (10) (2009) 1529–1532.
[10] Y. Sahoo, et al., J. Phys. Chem. B 109 (9) (2005) 3879–3885.
[11] R.M. Cornell, U. Schwertmann, The Iron Oxides, second ed., WILEY-VCH GmbH & Co. KGaA, Weinhein, 2003.
[12] J. Liu, et al., Angew. Chem. Int. Ed. 48 (32) (2009) 5875–5879.
[13] E. Munnier, et al., Int. J. Pharm. 363 (1–2) (2008) 170–176.
[14] M.E. Khosroshahi, L. Ghazanfari, Phys. E: Low-Dimensional Syst. Nanostruct 42 (6) (2010) 1824–1829.
[15] D. Yang, J. Hu, S. Fu, J. Phys. Chem. C 113 (18) (2009) 7646–7651.
[16] S. Chandra, et al., New J. Chem. 34 (4) (2010) 648–655.
[17] Y-h. Zheng, et al., Mater. Res. Bull. 41 (3) (2006) 525–529.
[18] Y. Li, H. Liao, Y. Qian, Mater. Res. Bull. 33 (6) (1998) 841–844.
[19] S. Park, J. Solid State Chem. 182 (9) (2009) 2456–2460.
[20] J.L. Cain, et al., J. Magn. Magn. Mater. 155 (1–3) (1996) 67–69.
[21] K. Mondal, et al., Fuel Process. Technol. 86 (1) (2004) 33–47.
[22] P. Jian, et al., J. Membr. Sci. 284 (1-2) (2006) 9–16.
[23] S. Xuan, et al., J. Magn. Magn. Mater. 308 (2) (2007) 210–213.
[24] J. Yan, et al., Colloids Surf. A: Physicochem. Eng. Aspects 340 (1–3) (2009) 109–114.
[25] X.-F. Qu, et al., J. Phys. Chem. C 114 (1) (2009) 284–289.
[26] W.S. Lu, et al., J. Magn. Magn. Mater 322 (13) (2010) 1828–1833.
[27] B.D. Cullity, second ed., Elements of X-Ray Diffraction, vol. 1, Addison-Wesley, 1996.
[28] M. Kallumadil, et al., J. Magn. Magn. Mater. 321 (10) (2009) 1509–1513.
[29] U. Schwertmann, E. Murad, Clays Clay Miner. 31 (4) (1983) 277–284.
[30] B. Sulzberger, et al., Marine Chem. 28 (1–3) (1989) 127–144.
[31] E. Tronc, et al., Langmuir 8 (1) (1992) 313–319.
[32] R. Muller, et al., J. Phys. Condens. Matter 18 (38) (2006) S2527–S2542.
[33] M. Racuciu, D.E. Creanga, A. Airinei, Eur. Phys. J. E 21 (2) (2006) 117–121.
[34] M. Rozman, M. Drofenik, J. Am. Ceramic Soc. 78 (9) (1995) 2449–2455.
[35] A. Goodarzi, et al., Mat. Res. Soc. Symp. Proc. 789 (2004). N.6.6.1-N.6.6.6.
[36] M. Nidhin, et al., Bull. Mater. Sci. 31 (1) (2008) 93–96.
[37] B.D. Cullity, Introduction to Magnetic Materials, first ed., Addison Wesley, New York, 1972.
[38] A.G. Roca, et al., J. Phys. Chem. C 111 (50) (2007) 18577–18584.
[39] R. Hergt, et al., J. Phys. Condens. Matter 18 (38) (2006) S2919–S2934.
[40] R. Hergt, et al., IEEE Trans. Magn. 34 (5 pt 2) (1998) 3745–3754.
[41] R. Hergt, S. Dutz, M. Rider, J. Phys. Condens. Matter 20 (2008) 38.
[42] J.-P. Fortin, et al., J. Am. Chem. Soc. 129 (9) (2007) 2628–2635.
[43] R. Hergt, et al., J. Magn. Magn. Mater. 270 (3) (2004) 345–357.